

A Pressure Sensory System Inspired by the Fish Lateral Line: Hydrodynamic Force Estimation and Wall Detection

Yiming Xu and Kamran Mohseni, *Senior Member, IEEE*

Abstract—Studies have shown that many behavioral decisions of fish are facilitated by the lateral line system which provides hydrodynamic information about the surrounding fluid. Inspired by the functionality of the system, a distributed pressure sensory system is developed. The system is intended for use on autonomous underwater vehicles to aid station keeping and accurate maneuvering by allowing the vehicle to react to the changes in the fluid environment before they result in body perturbation. The system can also be used for mission level decision making such as obstacle detection. This paper presents a prototype sensory system using differential, as opposed to absolute or gauge, pressure sensors as the sensing elements, which allows for higher measurement precision. Experimental tests are designed to characterize the system's ability to estimate the hydrodynamic force and to detect the presence of a wall. The hydrodynamic force estimated by the system is validated with an independent force measuring apparatus. The impending wall could also be detected by analyzing the pressure distribution obtained from the sensory system. Particularly, it is found that the wall distance and angle may be inferred by comparing the amplitude and phase of the Fourier components in the pressure distribution against those without the obstacle.

Index Terms—Aquatic robots, pressure sensors, robot sensing systems, sensor arrays, signal analysis.

I. INTRODUCTION

FOUND in most fish and some other aquatic organisms, the lateral line is a common mechanosensory system [1], [2] that serves an important role in various behaviors including station holding [3], rheotaxis (the ability to orient parallel to a flow field) [4], schooling [5], prey detection and capture [6]–[8], and social communication [9]. The neuromast, a mechanoreceptive structure, is believed to be responsible for the functionality of the lateral line. Specifically, as illustrated in Fig. 1, superficial neuromasts located on the body surface and protruding into the external fluid respond to steady and low-frequency components in the flow in proportion to the net velocity. Canal neuromasts

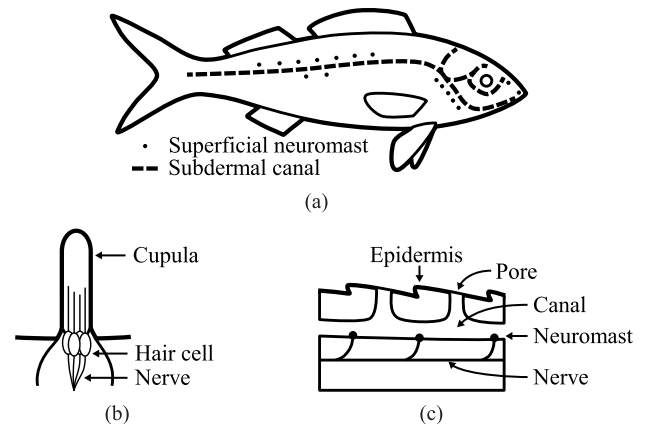


Fig. 1. (a) Schematic of a typical layout of the lateral line in a fish. (b) Schematic of the superficial neuromasts that are located on body surface and respond to low-frequency components and net velocity. (c) Schematic of the canal neuromasts that are inside subdermal canals and respond to high-frequency components and net acceleration of the flow. The figure is recreated from [20].

situated in subdermal canals along the lateral lines respond to high-frequency components, and react proportionally to the net acceleration (or the pressure gradient) [8], [10], [11]. In effect, by detecting water motions and pressure gradients in the surrounding environment, the lateral line system provides hydrodynamic information that in turn facilitates many behavioral decisions.

This paper demonstrates a pressure sensory system inspired by the lateral line for hydrodynamic sensing and detection. The objective of this study is to eventually implement and test the sensory system on the autonomous underwater vehicle prototype CephaloBot [12], as shown in Fig. 2(a). The vehicle is equipped with cephalopod-inspired vortex ring thrusters that can provide quantized propulsive force by creating arrays of high-momentum vortex rings with successive ingestion and expulsion of water [13], [14]. The device allows the vehicle to perform accurate maneuvers at low speed, without sacrificing its low-drag streamline profile for efficient high-speed traveling [15]–[17]. The design concept of the pressure sensory system is to create distributed arrays of sensors on the vehicle body for hydrodynamic force estimation as well as a linear, dense sensor arrangement at the front for detection of obstacles, as illustrated in Fig. 2(b).

To date, increasing research efforts have been devoted to replicating the sensing capabilities of the lateral line system.

Manuscript received January 12, 2016; revised August 28, 2016; accepted September 20, 2016. Date of publication October 19, 2016; date of current version July 12, 2017. This work was supported by the U.S. Office of Naval Research.

Associate Editor: B. Bingham.

Y. Xu is with the Department of Mechanical and Aerospace Engineering, University of Florida, Gainesville, FL 32611 USA (e-mail: yxu@ufl.edu).

K. Mohseni is with the Department of Mechanical and Aerospace Engineering, the Department of Electrical and Computer Engineering, and the Institute for Networked Autonomous Systems, University of Florida, Gainesville, FL 32611 USA (e-mail: mohseni@ufl.edu).

Digital Object Identifier 10.1109/JOE.2016.2613440

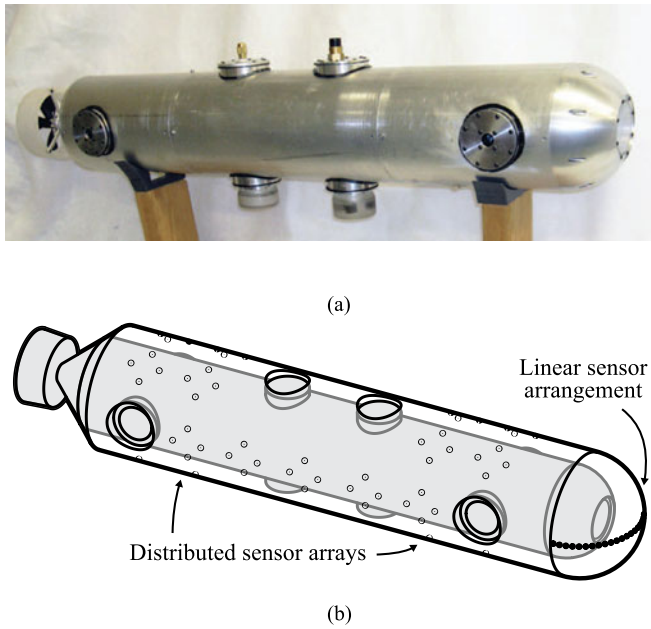


Fig. 2. (a) Autonomous underwater vehicle prototype CephaloBot. The vehicle is equipped with a rear propeller for propulsion and four vortex ring thrusters on both sides for turning maneuvers. Radio frequency and acoustic transmitters are utilized for communication and localization. The pressure sensory system under development will be installed and tested on this platform. (b) Design concept of the pressure sensory system. Distributed arrays of pressure sensors on the body of the vehicle provide hydrodynamic force estimation, whereas the linear arrangement of pressure sensors at the front of the vehicle could aid obstacle detection and avoidance.

Some researchers develop delicate sensory systems with micro-fabricated artificial sensors to mimic the structural features of the biological lateral line system, and study the sensory behaviors in various flow conditions. For example, in [18] and [19], miniature lateral line sensors are designed based on the thermal hot wire anemometry principle, and are tested for localizing dipole sources and identifying the hydrodynamic signature of wakes. The task of dipole localization is also achieved with micro-machined artificial hair sensors [20]. Additionally, optical flow sensors are developed as in [21] to detect water motions inside artificial lateral-line-like canals and are utilized to detect the wake behind moving objects. Polymer microelectromechanical pressure sensors are developed and tested in [22] to estimate the velocities of moving objects and to investigate the differences in pressure signals while the object is traveling at various distances. In [23], bioinspired microelectromechanical canal sensors are implemented to sensing various flow velocities. In [24], a combination of ionic polymer metal composite sensors and embedded pressure sensors are developed and tested for estimating flow velocity and angle of attack for rheotactic and station holding control. Additionally, biomimetic superficial neuromast structures with an artificial cupula is developed in [25] and [26], demonstrating an improved sensitivity. Refer to [27] for an in-depth review.

On the other hand, some other researchers utilize existing sensors in their tests, aiming at imitating the functionality of the biological lateral line systems. For instance, in [28], pressure sensors are used to identify the flow signature from static and moving cylinders with different cross sections; in [29], parallel

arrays of pressure sensors are deployed in a von Kármán vortex street to characterize the hydrodynamic features; and in [30], a pressure sensor array is used to identify the angle of attack of an underwater vehicle with respect to a freestream flow for rheotaxis control feedback. Other examples include using pressure sensors to estimate flow velocity and direction [31], [32] and to identify a wake and the size of its source [33].

In this study, the lateral-line-inspired sensory system also utilizes commercially available pressure sensors to investigate the mechanisms of hydrodynamic sensing, so that specialized lateral line sensors could be readily incorporated into the system if they become available in the future. One of the distinctive features of the system is that the commercially available pressure sensors are differential (as opposed to absolute or gauge) and measure the pressure differences between their two ports. This allows the choice of more sensitive sensors because the selection of the sensing range will not be restricted by the hydrostatic pressure that changes with depth, but only depends on the expected pressure gradients due to the depth difference between the two measuring ports and the fluid dynamics. In previous work from the group, potential flow models were set up to investigate the sensor response to various external excitation. The flow properties around a fish-shaped body are studied in the presence of a von Kármán vortex street. It is found that the position, velocity, and strength of the vortices can be recovered from the lateral line system [34]. Furthermore, wall detection is also investigated theoretically based on the hydrodynamic pressure distribution around the fish-shaped body [35]. Although the body shape is different from the one investigated in this paper, many of the pressure distribution features are in agreement.

To verify the results obtained from hydrodynamic simulation, experimental tests are designed to realize the simulation cases. In the experiment, two separate cylindrical bodies outfitted with the sensory system are towed through water to recreate the test scenarios in the simulation for force estimation and wall detection. The experimental setup includes a sliding cart structure, a motorized pulley system that propels the motion at a controlled speed, and a motion capture system providing accurate position measurements. In this paper, the testing results for both hydrodynamic force estimation and wall detection are illustrated and analyzed. In the force estimation test, the pressure sensory system captures the variations in the hydrodynamic forces when the system undergoes unsteady motions through water. The estimation is validated by independent force measurement. In the wall detection test, the system is able to distinguish differences in surface pressure distribution between approaching a wall versus moving in open water. The wall distance and angle with respect to the moving direction are determined from the differences in the pressure signals.

II. EXPERIMENTAL SETUP

The experimental setup for the sensory system consists of the vehicle mockups as test subjects with integrated pressure sensors, the mechanical and electrical systems that support the motions of the subjects, and the additional sensory system that provides the independent reference. This section will first introduce the pressure sensors used in the system, and subsequently present the supporting facilities.

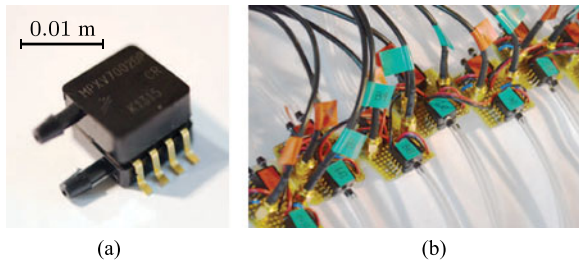


Fig. 3. (a) Differential pressure sensor used in the system. (b) Sensor connections. Powered by 5-V direct current (dc), the sensor measures pressure difference up to ± 2 kPa between the two ports. Analog signals are sent through shielded SubMiniature-A (SMA) cables.

A. Pressure Sensors

The sensing elements of the system are commercially available monolithic silicon pressure sensors, MPXV7002DP. These piezoresistive transducers provide differential pressure measurements between their two ports with a sensing range from -2 to 2 kPa. The transfer function from the pressure measurement P to the output voltage V_{OUT} can be written as

$$V_{OUT} = (0.2 \text{ kPa}^{-1} P + 0.5) V_S \pm 2.5\% V_{FSS} \quad (1)$$

where the nominal supply voltage is $V_S = 5.0$ V and the full-scale voltage span is $V_{FSS} = 4.5$ V.

Pictures of the sensors are shown in Fig. 3. During the tests, the analog signals are fed into the data acquisition card (NI PCI-6229) via shielded SubMiniature-A (SMA) cables. The signals are sampled at 1 kHz, and converted with 64-b precision. While the system is in operation, the noise in the pressure signals is about 6 mV, corresponding to a magnitude of about 6 Pa in pressure. Possible sources of noise include acoustic noise or vibrations that would affect the piezoresistive transducer and electrical noise introduced by the power supply, cable connections, and the data acquisition process. To eliminate the signal offset due to the mechanical stress and mounting position from installation, the average zero-pressure voltage is subtracted from the signal for every sensor before experiments.

The pressure measurements are validated by placing the individual sensor ports at various depths in water and comparing the measured pressure differences with the expected ones. This comparison is shown in Fig. 4. The pressure error bars represent the standard deviation of the water depth measurements. The voltage error bars are from the standard deviation of voltage samples from 20 pressure sensors. The solid and dashed lines depict the nominal transfer function and the precision bound, respectively. Comparison between the sensory measurement and the precision bound shows that the performance of the pressure sensors is satisfactory.

B. Testing Facilities

The purpose of the testing apparatus is to carry the testing subjects—cylinders integrated with pressure sensors—through water at a designated speed, and to collect their position and velocity information.

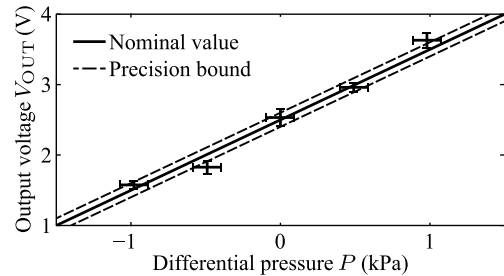


Fig. 4. Voltage outputs from sensors with various pressure differences. The pressure variation is obtained from different water depths. Pressure (horizontal) error bounds represent the standard deviation of the water depth measurements. Voltage (vertical) error bounds are from the standard deviation of voltage samples from 20 pressure sensors. The solid and dashed lines depict the nominal transfer function and the precision bound, respectively.



Fig. 5. Testing tank and loading platform. The tank is a 4.6-m (15-ft) tall, 8-m (26-ft) diameter, and 250-m^3 (65 000-gal) capacity cylindrical water reservoir. The platform spans on top of the tank. The six cameras for the motion capture system are installed at the bottom of the tank, fixing the field of view toward the area next to the platform.

The testing cylinders are made from 6-in Schedule-40 polyvinyl chloride (PVC) pipes with an outer diameter of 16.8 cm (6.625 in) and a wall thickness of 7.54 mm (0.297 in). Before being submerged in water, the cylinders are loaded with lead shot weights to achieve neutral buoyancy. The pressure sensor ports are connected to the openings on the cylinder surface with 2.38-mm (0.0937-in) inner diameter flexible vinyl tubes. Two separate testing cylinders are designed specifically for the force estimation and the wall detection tests, whose designs will be detailed in Sections III and IV, respectively.

The test apparatus is set up in a cylindrical water tank with a depth of 4.6 m (15 ft), a diameter of 8 m (26 ft), and a capacity of 250 m^3 (65 000 gal), as shown in Fig. 5. A platform I-beam (with a flange width of 20 cm or 8 in and a section depth of 20 cm or 8 in) is utilized as a track for the linear motion driver. A carrying cart is manufactured to support the testing subjects, while clamping tightly and sliding along the I-beam, as shown in Fig. 6.

The sliding cart is either pulled manually or actuated by a motorized pulley system. Positioned at each end of the I-beam, the pulley system drives the cart at a controlled speed with

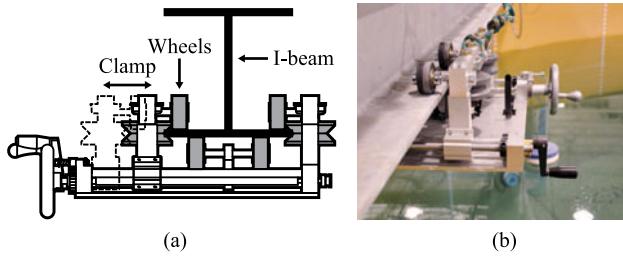


Fig. 6. (a) Drawing of the sliding cart. (b) Cart setup. The cart has three sets of rubber wheels to clamp onto the flange from top and bottom, four grooved wheels to restrict sideways motions, and a connector to support the testing subjects. The clamping mechanism allows for easy attachment and detachment of the cart to and from the I-beam.

steel cable wires. One pulley is connected to a motor. The motor is a brush-commutated direct current (dc) motor (Pittman ID33005-SP) that produces a continuous output torque of 0.85 N·m (120 oz·in) at 6000 r/min. The rotation of the motor is monitored by an encoder at the motor shaft, and the rotational speed is controlled by a proportional–integral–derivative feedback controller.

The position of the testing subjects is measured with a motion capture system, where six underwater cameras (Oqus 5-series from Qualisys) provide the 3-D positions of reflective markers placed on the testing subjects. The camera system records the positions of the markers at 100 frames/s, and has a spatial resolution of about 1 mm after calibration.

III. FORCE ESTIMATION TEST

Traditionally, the control performance of underwater vehicles is analyzed in static flow conditions with perturbations about some nominal traveling speed [36]. Hydrodynamic forces due to acceleration and velocity of the vehicle are modeled as added mass terms and viscous damping terms, respectively. Coefficients of these terms are usually obtained based on linearization around a nominal operation state of the vehicle. Influences from the nonstatic background flow are often considered as additional disturbances. This conventional treatment is undoubtedly limited in modeling accuracy for control purposes, especially for underwater vehicles with high maneuverability in an unsteady flow environment. With the motivation to improve the vehicle's control performance, a hydrodynamic force estimation algorithm is developed in [37]. The algorithm utilizes measurements from distributed pressure sensors to estimate the hydrodynamic forces and moments acting on the vehicle, providing hydrodynamic information about the surrounding flow.

The hydrodynamic force estimation algorithm is tested in experiment. The concept of the test is that for an object moving in water, the linear (or angular) acceleration multiplied by mass (or moment of inertia) of the object is equal to the resultant external force (or torque) including the hydrodynamic force (or moment) and the force (or moment) from the structure supporting the object. On the one hand, the hydrodynamic force and moment can be estimated with pressure sensors on the surface of the object; and on the other hand, the same quantities can be calculated based on the object's acceleration and other supporting forces

and moments acting on the object, which are measured by the motion capture system and the strain gauges, respectively.

A. Estimation Algorithm

When the testing subject is moving under water, the hydrodynamic forces and moments acting on the surface come from the water pressure applied on the surface of the vehicle. The shear forces are minimal and negligible because of the low Reynolds number. Using fitting techniques, the pressure difference measurements from sensors at multiple locations can be used to reconstruct the pressure distribution over the entire body. Thus, the total damping force and moment can be estimated by integrating the pressure distribution over the body profile. The resultant force estimation $\hat{\mathbf{f}}_D$ will take the form of linear, fixed weight combinations of the pressure measurements [37]

$$\hat{\mathbf{f}}_D = \int_{\mathcal{T}} \mathbf{b} \mathbf{K}_{MN}^T(\theta, \phi) r^2 d\theta d\phi \mathbf{K}_P \mathbf{P}. \quad (2)$$

The hydrodynamic damping forces and moments can be estimated as the pressure signal vector \mathbf{P} premultiplied by a matrix that is a function of the locations for the pressure sensors. Refer to [37] for details of the algorithm. Once the sensor locations are defined, the matrix can be obtained *a priori*. Thus, the force estimation can be computed effortlessly. The experiment is aimed at validating this force estimation algorithm.

B. Force Estimation Setup

The specific experimental setup, as illustrated in Fig. 7(a), consists of a horizontal cylinder, a vertical rod, and an attaching structure to the sliding cart. The cylinder is made from a PVC pipe which is 81.3 cm (32 in) long and is closed at both ends with rounded caps, so that it resembles the shape of an underwater vehicle. In the test, the cylinder is submerged under water, and the slider carries the cylinder with the rod. Hydrodynamic pressure is measured on the surface of the cylinder, the force and moment acting on the cylinder as transmitted through the connecting structure are obtained with strain gauges on the rod, and the acceleration of the cylinder (used to calculate inertial forces) is calculated from the position measurements with the motion capture system.

There are in total 20 sensors in the pressure sensory system, as shown in Fig. 7(b). Generally, the pressure sensors need to be distributed around the cylinder to reconstruct the pressure distribution for force estimation. In this particular test, the differential pressure sensors are arranged in an array that covers half of the cylinder surface, based on the assumption that the pressure distribution is symmetric when the cylinder is moving perpendicular to its central axis. The sensors are grouped in pairs of two; one measures the pressure difference along the longitudinal direction, while the other measures the difference along the circumferential direction. Together, they form a 5×2 array.

The force and moment acting on the cylinder by the connecting rod is measured by strain gauges. The rod is made from an aluminum pipe with a 2.54-cm (1-in) diameter. In total, 16 strain gauge elements form four Wheatstone bridges on the surface of

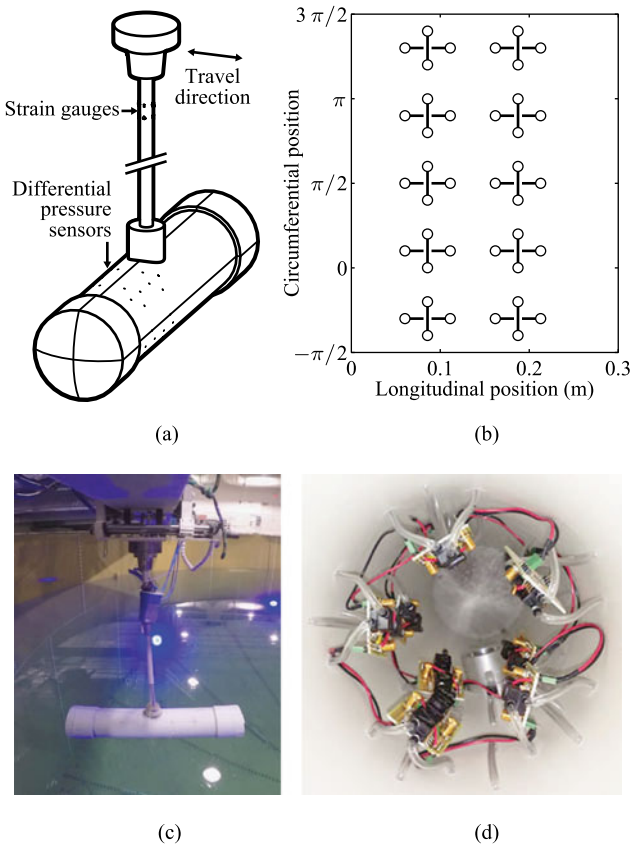


Fig. 7. (a) Schematic of the force estimation experimental setup. (b) Sensor arrangement drawing. (c) Testing cylinder on the slider. (d) Sensors inside the testing cylinder. In total, 20 pressure sensors are installed with the ports connected to the surface of the cylinder. The sensors are grouped into pairs; one sensor measures the pressure difference along the longitudinal direction, while the other measures the difference along the circumferential direction. Each group of two connected circles represent two ports of a sensor. The rod supports the cylinder and protect the signal cables within. On the rod there are strain gauges that measures the strain, which relates to the force and moment acting on the cylinder by the rod itself.

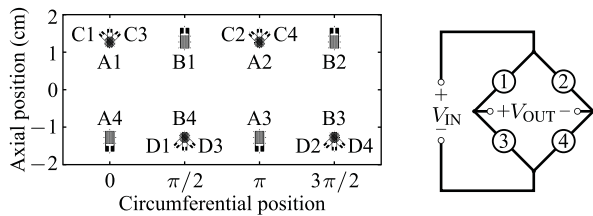


Fig. 8. (a) Schematic of the strain gauge arrangement. (b) Wheatstone bridge circuit. The 16 strain gauges form four Wheatstone bridge circuits labeled from A to D. After calibration, circuit A (B) measures the horizontal force along (perpendicular to) the travel direction, whereas circuits C and D measure the horizontal torque with strain gauges placed at 45° from the axial direction.

the pipe, as illustrated in Fig. 8. Two bridges (A and B) measure the bending strain along two perpendicular directions, while the other two groups (in circuits C and D) are placed at an angle of 45° from the axial direction and measure the torsional strain. Once calibrated, the strain gauge circuits measure the force and moment acting on the cylinder by the rod. Furthermore, to reduce the deviation from the cylindrical shape, the sensor power and signal cables are threaded through the aluminum pipe be-

fore being connected to the data acquisition system. While the cylinder is moving along the slideway, its position is recorded with the motion capture system, and the acceleration can be obtained through signal processing.

C. Test Results

The testing system was translated across the tank with multiple trajectories while independently collecting data from the pressure sensors and the strain gauges, as well as recording the global position of the cylinder from the motion capture system. In each test, the system starts from rest and accelerates to a constant speed before it decelerates back to a stop. The pressure distribution is assumed to be symmetric between the two ends of the cylinder. Filtered and calibrated signals together with the force estimation results from two tests are shown in Fig. 9. The velocity is roughly maintained around 0.1 m/s with intentional variations to achieve varying acceleration, which resembles the type of motions performed by the underwater vehicle while docking. Once the controlled motion stops, the cylinder starts a damped oscillation due to the motion of the water and the elasticity in the rod. As shown in the results, the estimated hydrodynamic force generally captures the variations in the measurement, which verifies the estimation algorithm. The estimation results are summarized in Table I. In four sets of tests, the standard deviation of the estimation error is about 0.8 N. Note that in this particular test, the geometry and the motion of the setup are symmetric, hence the symmetry in the pressure distribution. For a general case on an underwater vehicle, pressure sensors need to be distributed across the vehicle surface for a correct estimation of the hydrodynamic force and moment in all directions. In addition, a denser sensor arrangement may be necessary to accurately resolve a more complex pressure distribution due to flow separation and vortex shedding.

IV. WALL DETECTION TEST

Beside the hydrodynamic force estimation, another capability of the sensory system is also investigated. The biological lateral line system is believed to be able to sense the flow field altered by the presence of nearby objects, and therefore enables the fish to detect impending obstacles [38]. Unlike the force estimation where the pressure distribution is globally integrated, obstacle detection focuses instead on the local characteristics of the pressure distribution. The presence of an obstacle confines and accelerates the escaping flow and results in a high-pressure region toward the direction of the obstacle, and the magnitude of the pressure is related to the distance to the obstacle. By comparing the pressure distribution to that of an open environment, information about the obstacle could be obtained. This section first summarizes a test case in a 2-D space for numerical simulation, then describes the experimental test that realizes the 2-D test case in the water tank, and finally concludes with illustration and analysis of the test results.

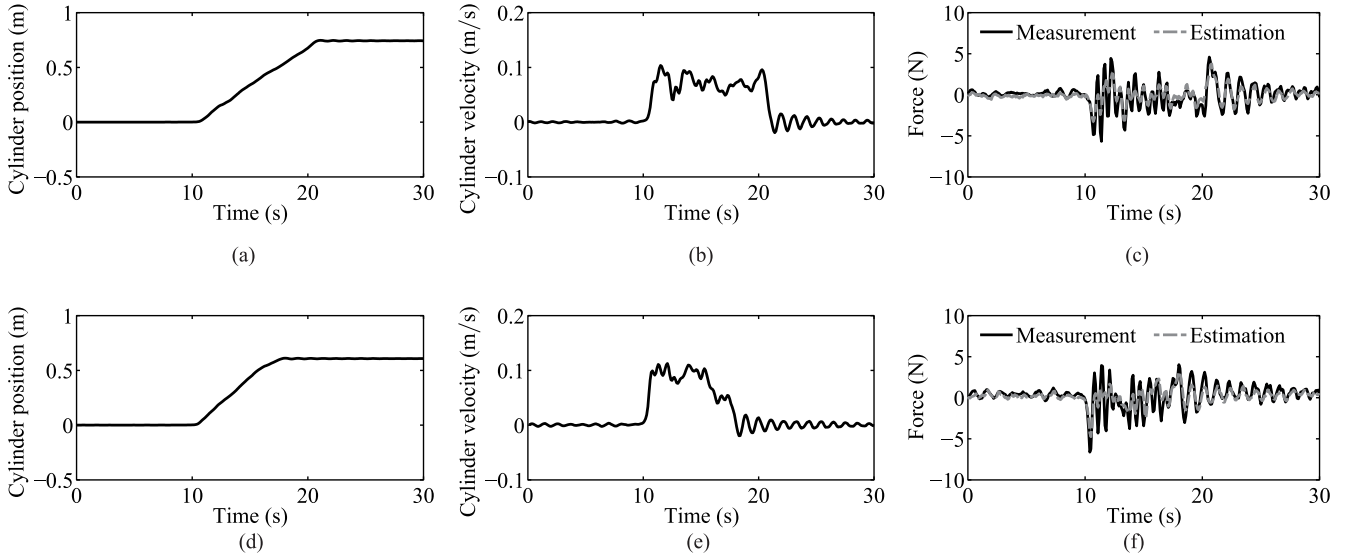


Fig. 9. (a)–(c) Plots of cylinder position, velocity, and hydrodynamic force estimation results for Test 1. (d)–(f) Plots for Test 2. In each test, the cylinder starts from rest and is manually pulled along the slideway before it decelerates to a stop. Pressure measurements are collected around the surface of the cylinder and are formulated into the hydrodynamic force estimation. The estimated force is compared to the measurement based on the force from the strain gauges and the acceleration from the motion capture system.

TABLE I
SUMMARY OF FORCE ESTIMATION RESULTS

Test	Estimation error (N)		Reference force (N)	
	Std.	Max.	Std.	Max.
1	1.03	2.16	2.36	6.82
2	0.86	2.97	2.16	8.42
3	0.98	3.51	2.00	5.97
4	0.63	1.05	1.42	4.60

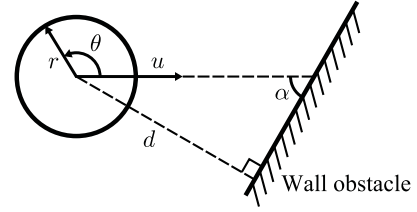


Fig. 10. Diagram of the wall detection model. A circular sensing system with radius r approaches the wall at a speed of u . Circumferential position on the circle is denoted by θ . The distance to the wall and the wall angle are defined as d and α , respectively.

A. Detection Model

Generally, detecting obstacles using hydrodynamic sensory systems depends on the flow field generated by the motion of the system and the way this flow field is altered by the presence of the obstacles. For the purpose of demonstration, a simple 2-D case is defined: the sensory system is distributed on a circular surface and is moving along a straight line in an ambient fluid toward a straight wall as the obstacle. It is worth noting that although this circular model is simpler than the fish-shaped body studied in simulation in [35], many of the pressure distribution features are similar and the experimental results in this paper could aid further development of a wall detection algorithm.

As illustrated in Fig. 10, the radius of the circle is defined to be r . The angle between the velocity vector and the wall boundary is denoted as α and the distance to the wall from the center of the circle is denoted by d . As the circle moves at a speed of u , the flow properties around its circumference will be affected by the existence of the obstacle. Therefore, with the assumption that the hydrodynamic pressure is measurable on the circle, the pressure distribution may be analyzed to obtain information about the wall including its existence, the distance d , and the wall angle α .

Assuming that the flow is inviscid, incompressible, and irrotational, a 2-D potential flow model is set up to study the pressure distribution around the circle. The analytical solution for the pressure distribution in the case that the distance to the wall approaches infinity, i.e., $d \rightarrow \infty$, is the classical potential flow around a circular cylinder. The pressure P at circumferential position θ can be expressed as

$$P(\theta) = \rho u^2 \cos(2\theta) - \frac{1}{2} \rho u^2 + P_\infty \quad (3)$$

where ρ represents the density of the fluid, and P_∞ denotes the stagnation pressure. The pressure reaches the maximum at the front and rear stagnation points of the circle when $\theta = 0$ and π , and arrives at the minimum on both sides when $\theta = \pm\pi/2$. However, finding the analytical solution for the nontrivial cases is almost intractable. Therefore, numerical techniques are used to calculate the pressure distribution for several different cases, while (3) is used as a reference for the open environment case without obstacles.

Specifically in the numerical computation, a potential flow model is developed to describe the flow field which is assumed to be incompressible, irrotational, and inviscid. The flow field contains continuous vortex sheets on the boundaries of the

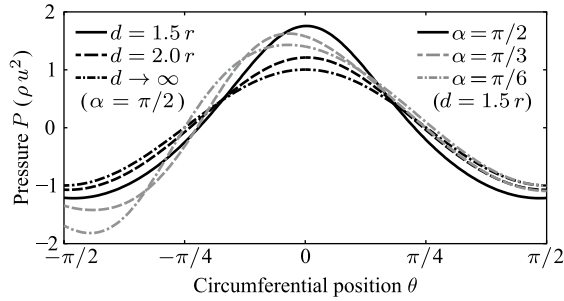


Fig. 11. Numerical results of the pressure distribution in the front of the circle as it approaches toward a wall at different angles. The pressure is normalized by the quantity ρu^2 after subtraction by the mean pressure value. As the circle comes closer to the wall, the pressure in the front becomes higher, and the high-pressure region shifts toward the wall side, if the wall is not perpendicular to the moving direction, i.e., $\alpha \neq \pi/2$.

circular body and the straight wall to enforce the no-penetration condition. Discretizing the vortex sheets into individual vortex panels with uniform strengths yields a panel method formulation of the problem. As a result, the flow field can be obtained by solving for the vortex panel strengths under the boundary condition. Additionally, the pressure distribution around the circle is calculated with the Bernoulli equation.

Fig. 11 shows the numerical results of the pressure distribution for various wall distances and angles. In this case, 400 and 800 vortex panels are placed on the boundaries of the circle and the straight wall, respectively. The pressure value is normalized by the quantity ρu^2 , and the average component is subtracted from the result. The presence of the wall forces the flow to accelerate around the circle and results in a high-pressure region toward the wall. The closer the circle comes to the wall, the higher the peak pressure value becomes. On the other hand, as the wall angle deviates from $\alpha = \pi/2$, the high-pressure region inclines toward the side of the wall. These are the two major features to be verified in the experimental tests.

B. Fourier Analysis

Since the hydrodynamic pressure varies around the circumference of the cylinder, the features of the pressure distribution may also be examined in the Fourier domain. In the open environment case without obstacles as in (3), there is only one Fourier component with a wave number of 2. Performing the Fourier transformation of the pressure distribution for the general case yields a Fourier spectrum with one dominant component at the wave number 2. The amplitudes of other components drastically decrease as the wave number departs from this dominant component. When the circle approaches the wall, the amplitudes of all components increase, which corresponds to the pressure increase. In addition, the phase angles of the Fourier components vary with the wall angle α , except for the dominant component whose phase angle barely changes. This corresponds to the shift of the high-pressure region due to the presence of the wall, while the phase of the dominant component is unaffected because the motion of the circle remains the same. By correlating the features in the Fourier spectrum to the wall distance d and angle α ,

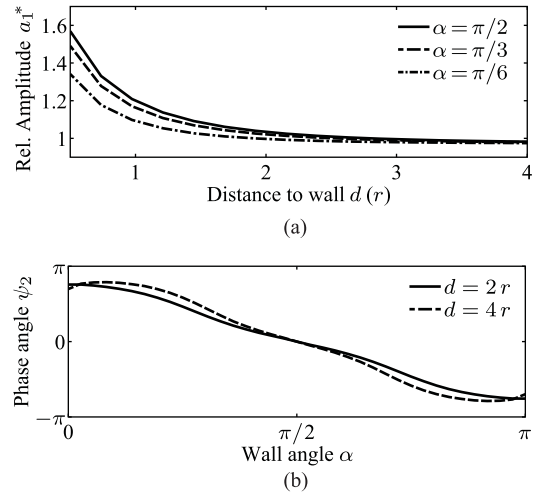


Fig. 12. (a) Relative amplitude α_1^* of wave number $\omega_1 = 2$ versus wall distance d . Compared to the case without the wall, the amplitude roughly varies in reciprocal proportion to the wall distance. (b) Phase angle ψ_2 of wave number $\omega_2 = 4$ versus wall angle α . The phase angle almost monotonically changes with the wall angle.

the amplitude reveals the wall distance d and the phase infers the wall angle.

In practice, there is only a finite number of sensors covering the front section of a circle. Therefore, the Fourier series can be used instead of the continuous transformation. The pressure function $P(\theta)$ can be written as

$$P(\theta) = a_0 + \sum_{k=1}^{\infty} a_k \cos(\omega_k \theta + \psi_k), \quad \theta \in [-\pi/2, \pi/2] \quad (4)$$

where a_0 denotes the dc component of the pressure function, and a_k and ψ_k denote the amplitude and phase of the periodic component with wave number $\omega_k = 2k$, respectively. In this way, the peak pressure magnitude and the shifting of the pressure peak are reflected by the amplitude a_k and the phase ψ_k of each Fourier component.

Accounting for the inevitable noise in the measurement and the amplitudes of the Fourier components, useful signals with the largest magnitudes are preferred for analysis. The amplitude of wave number $\omega_1 = 2$ and phase ψ_2 of the neighboring wave number $\omega_2 = 4$ can be considered for estimating wall distance d and angle α since they have the most significant signal magnitudes compared to the noise level. Fig. 12 illustrates that the relative amplitude a_1^* is approximately in reciprocal proportion to the wall distance d ; and that the phase angle ψ_2 is almost a monotonic function of the wall angle α , which can be approximated by

$$a_1^* \approx 0.27/d + 0.9, \quad \psi_2 \approx -1.81\alpha + 2.8. \quad (5)$$

These relationships from the simulation will be used as references in the experiment. However, the precision of this estimation depends on that of the sensors, which will be further discussed in Section IV-D.

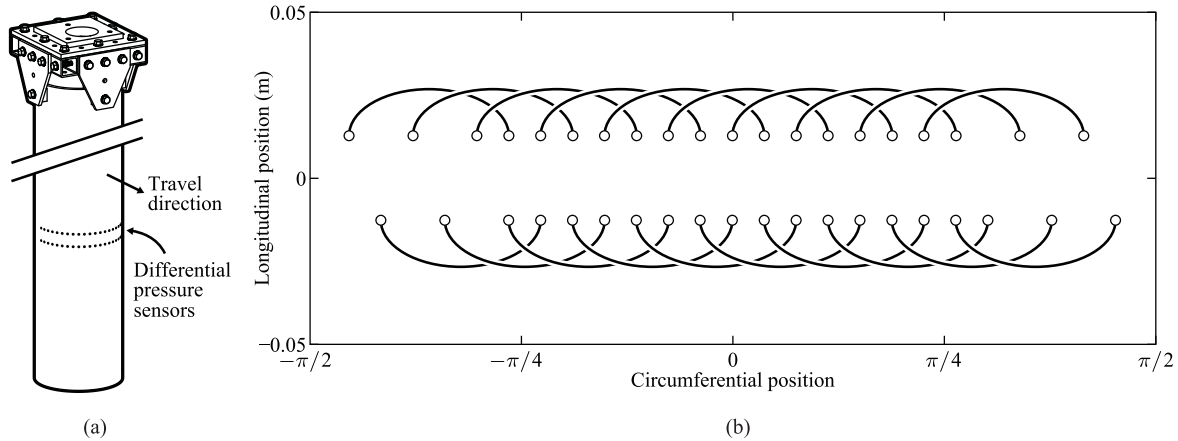


Fig. 13. (a) Schematic of the wall detection experimental setup. (b) Sensor arrangement on the vertically positioned cylinder. In total, 20 pressure sensors are installed with the sensor ports connected to the front-facing surface along the horizontal circumference. The sensors are connected in an interlaced manner to ensure sufficient stimulation for each sensor and an abundant number of sampling points.

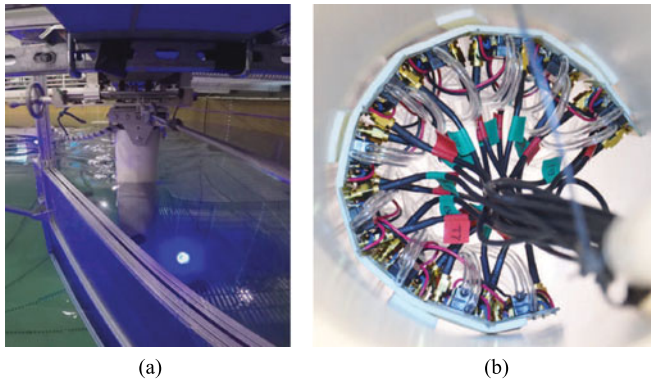


Fig. 14. (a) Wall detection test setup. (b) Sensor installation inside cylinder. The ports for the 20 pressure sensors are open along the circumferential direction in the front of the cylinder. The wall structure can be positioned at various angles. In each test, the cart carries the test cylinder towards the wall in a controlled motion and stops before contact with the wall structure.

C. Wall Detection Setup

The 2-D hydrodynamic model for wall detection can be realized in experimental tests. The setup includes a vertical cylinder and a wall structure, as depicted in Fig. 13(a). The cylinder is a 76-cm-long (30 in) PVC pipe with sensor ports around the middle circumference for 20 differential pressure sensors; see Fig. 13(b). When the cylinder is installed, the ports are about 32 cm (12.5 in) both from the bottom of the cylinder and to the water surface, in order to reduce surface influence and 3-D effects. The sensor openings are facing the front of the cylinder to avoid the flow separation and complex (and possibly turbulent) wakes. The interlaced sensor connection ensures that the differential sensors are receiving stimulation of sufficient magnitudes, while maintaining a reasonable number of sampling points. The wall is made from 1.2-m \times 1.2-m (48-in \times 48-in) PVC plates, with supporting structures that can be attached to the platform at various angles. Pictures of the sensory system and the test setup are shown in Fig. 14.

Three groups of tests are conducted with different wall angles $\alpha = \pi/2$, $\pi/3$, and $\pi/6$, respectively. In each group, the

cylinder is towed in a controlled motion toward the wall and is stopped before contact with the wall structure. After each group, the same motion is repeated without the wall structure for reference. Signals from the differential pressure sensors as well as the cylinder position is recorded and analyzed, as shown in Figs. 15–17.

For each test, the distance from the axis of the cylinder to the surface of the wall is computed with the position data from the motion capture system. The cylinder accelerates toward the wall and decelerates abruptly before running into a stopper in front of the wall structure. In total, five tests with the wall and five tests without the wall are conducted for each wall angle. One pair of tests with the minimal differences in the velocity profiles is selected for analysis in each group. Differential pressure data are filtered temporally and fitted to a Fourier series function along the circumferential direction as in (4). The pressure distribution during each test is depicted using contour plots. Between neighboring contour levels there is a pressure increment of 20 Pa, which is above the average noise level of 6 Pa. Since the pressure distribution beyond the angular position $\pm\pi/4$ may be affected by flow separation and fitting error, only the middle section will be analyzed.

D. Test Results

In Fig. 15, the test results with wall angle $\alpha = \pi/2$ (i.e., wall perpendicular to motion) are illustrated. The distance to the wall and the cylinder velocity in the selected pair of tests are shown in Fig. 15(a), to showcase the consistency between the testing cases. By comparing the pressure distributions between the case with wall angle $\alpha = \pi/2$ in Fig. 15(b) and the case without wall in Fig. 15(c), the difference in the pressure distribution is shown in Fig. 15(d). Before the cylinder stops in front of the wall (as marked by the dashed line in the contour plot), the pressure is relatively higher with the wall forcing the flow to accelerate around the cylinder, which agrees with the prediction from numerical simulation. Also, it can be found that the pressure distribution in both tests is more or less symmetric about the angular position $\theta = 0$ when comparing the pressure between

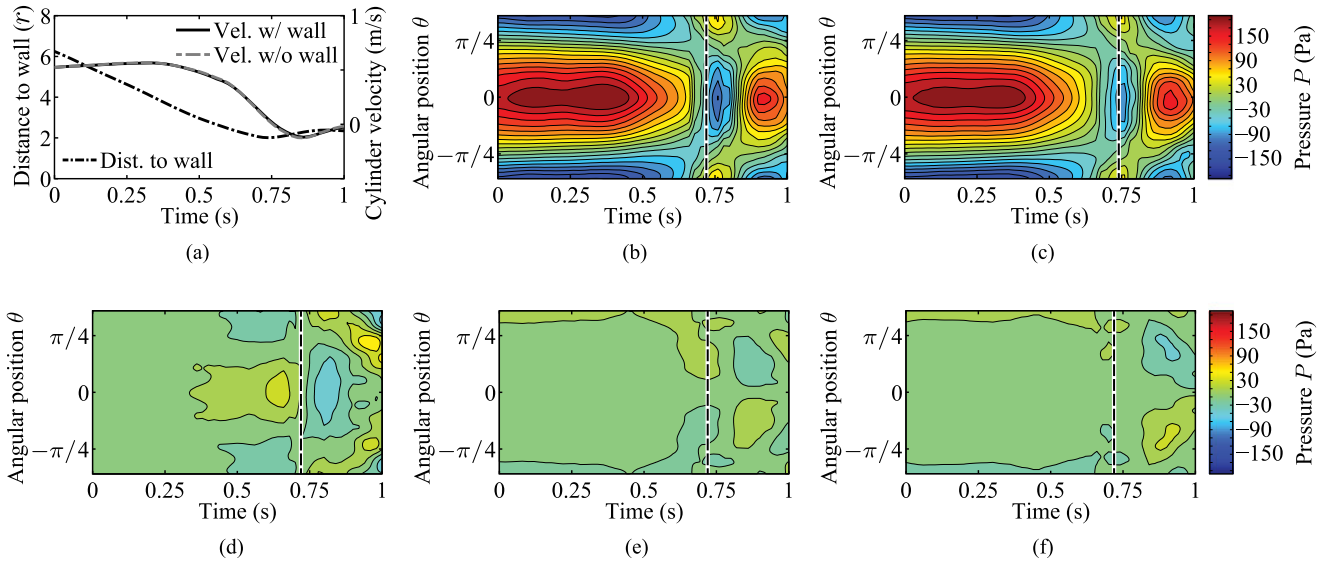


Fig. 15. Wall detection result comparison between wall angle $\alpha = \pi/2$ and the reference without the wall. (a) Cylinder distance from the wall and its velocity as a function of time. (b) Pressure distribution with the wall. (c) Pressure distribution without the wall. (d) Pressure contribution by the existence of the wall. (e) Asymmetric pressure with the wall. (f) Asymmetric pressure without the wall. Ignoring the pressure distribution beyond angular position $\pm\pi/4$ (which may be affected by flow separation, etc.) and after the cylinder stops (as indicated by dotted line), the existence of the wall increases the peak pressure as the cylinder approaches. The pressure distribution is more or less symmetric while the cylinder is in motion. There is a pressure increment of 20 Pa between neighboring contour levels.

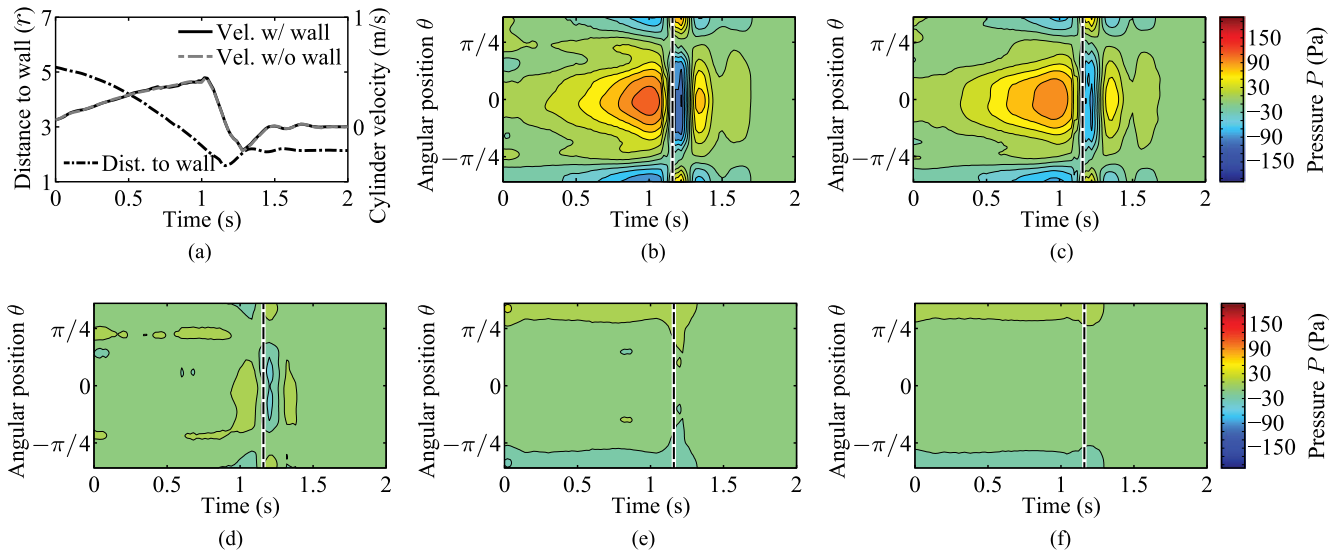


Fig. 16 Wall detection result comparison between wall angle $\alpha = \pi/3$ and the reference without the wall. (a) Cylinder distance from the wall and its velocity as a function of time. (b) Pressure distribution with the wall. (c) Pressure distribution without the wall. (d) Pressure contribution by the existence of the wall. (e) Asymmetric pressure with the wall. (f) Asymmetric pressure without the wall. The peak pressure slightly increases as the cylinder approaches the wall, and the positive pressure slightly inclines toward the wall side as compared to the reference.

the left and right sides, as shown in Fig. 15(e) for the wall angle $\alpha = \pi/2$ case and in Fig. 15(f) for the reference (no wall) case.

Similar conclusion can be reached for the groups with wall angle $\alpha = \pi/3$ and $\alpha = \pi/6$, as in Figs. 16 and 17. In addition to the change in (relative) pressure magnitude, the position of the pressure peak for these two groups is slightly inclined toward the side of the wall, because the presence of the wall increases the pressure by accelerating the flow between the cylinder and the wall. As the wall angle deviates away from the symmetric configuration $\alpha = \pi/2$, the asymmetric in the pressure distribution becomes more obvious, as depicted in Fig. 16(e) and

17(e). This also coincides with the trend from the numerical computation.

The results from the experimental tests imply that, as the cylinder moves in water, the existence of a wall can be inferred by comparing the pressure distribution with that of a “nominal” distribution in an open environment, and that the angle of the wall relative to the cylinder motion can be obtained by analyzing the asymmetry of the pressure distribution. The experiment and simulation results are compared in the Fourier domain in Fig. 18. Specifically, Fig. 18(a) shows the relationship between the relative amplitude a_1^* and the wall distance d for wall

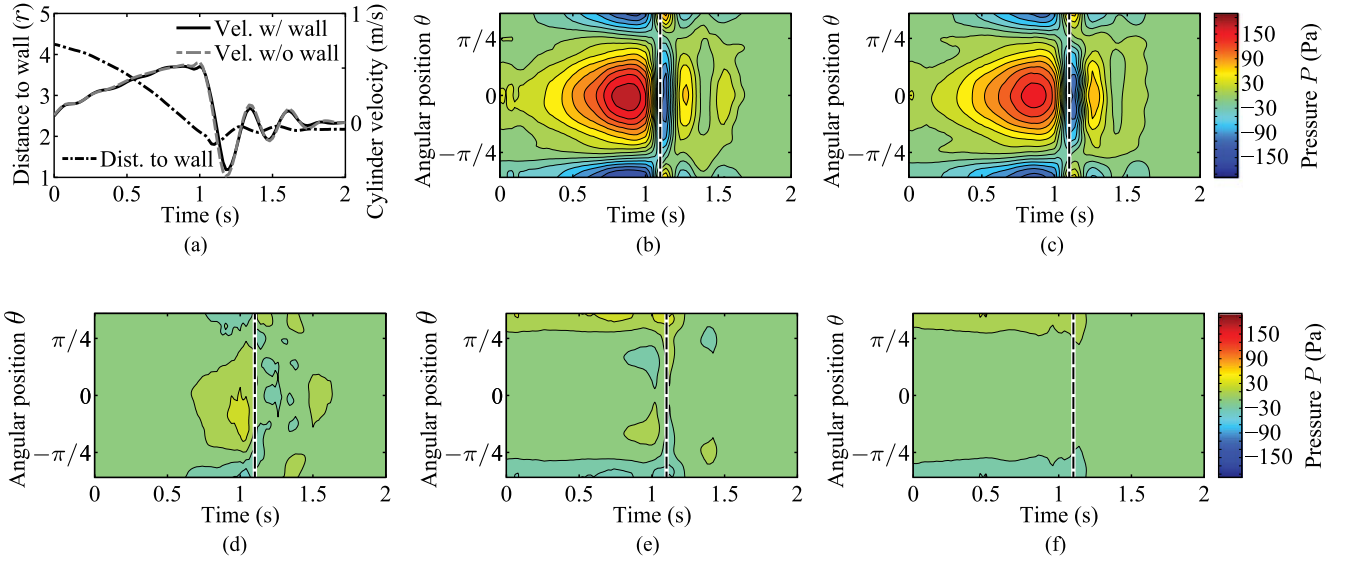


Fig. 17 Wall detection result comparison between wall angle $\alpha = \pi/6$ and the reference without the wall. (a) Cylinder distance from the wall and its velocity as a function of time. (b) Pressure distribution with the wall. (c) Pressure distribution without the wall. (d) Pressure contribution by the existence of the wall. (e) Asymmetric pressure with the wall. (f) Asymmetric pressure without the wall. The peak pressure increases as the cylinder approaches the wall, and the pressure distribution is obviously leaning toward the wall side as compared to the reference.

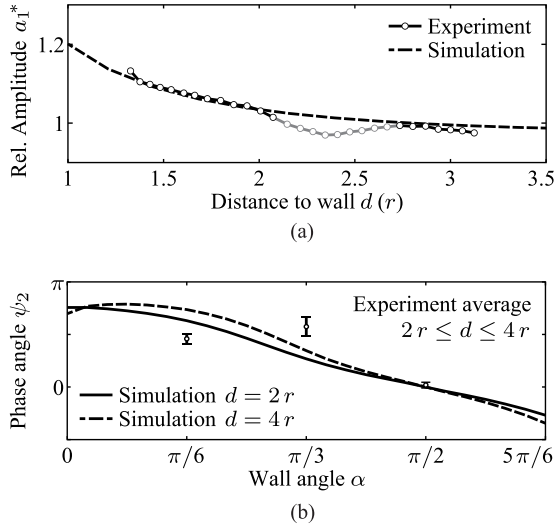


Fig. 18. Comparison of the pressure distribution between the simulation and experimental results. (a) Relative amplitude a_1^* of $\omega_1 = 2$ component versus wall distance d . The relative amplitude is obtained from one pair of tests and it generally follows the trend from the simulation, except for the region where the velocity profiles have slight discrepancies between the cases with and without the wall (wherefore the relative amplitude is less accurate as colored in gray). (b) Phase angle ψ_2 of $\omega_2 = 4$ component versus wall angle α . The phase angle is the average among five pairs of tests and it roughly agrees with the prediction from simulation. The angle correspondence is less precise for the wall angle $\alpha = \pi/6$ and $\pi/3$ because the magnitude of the corresponding component α_2 is close to the signal noise level.

angle $\alpha = \pi/2$ from one pair of tests with the best velocity profile match between the cases with and without wall. The experimental data generally follow the trend predicted by the simulation, except for a region (colored in gray) where the velocity profiles of the cylinder have a slight discrepancy. Since the pressure magnitude is roughly quadratic in the cylinder velocity, larger difference between the estimation and the reference may be expected when the velocity profiles are not aligned. Fig. 18(b)

depicts the correspondence between the phase angle ψ_2 and the wall angle α . The experimental data are obtained from the average of five pairs of tests and loosely follows the simulation results, which is reasonable because the wave number ω_2 components normally have a smaller magnitudes (therefore, lower precision) as compared to those of wave number ω_1 . Additionally, the amplitude a_2 of the wave number ω_2 component becomes smaller as the wall angle deviates away from $\alpha = \pi/2$. In fact, it comes around the sensor noise level for the data points with wall angle $\alpha = \pi/6$ and $\pi/3$, which might explain the data points being further away from the reference than the wall angle $\alpha = \pi/2$ case.

Applying the approximation functions in (5), the wall distance and angle could be inferred from the relative amplitude a_1^* and phase angle ψ_2 . The estimation during five pairs of tests is compared with the reference in Fig. 19. Particularly, in Fig. 19(a), the wall distance estimation data are based on the average among five pairs of tests to accommodate the discrepancy in the velocity profile for each individual pair of tests. As a result, the wall distance estimation (including the velocity profile mismatch) has a standard deviation of $0.83 r$ (as illustrated by the gray solid lines). In Fig. 19(b), data points for the wall angle estimation are obtained from the average among five pairs of tests for different wall angles. Based on the sensor noise in the experiment, a varying error bound is also provided with respect to different wall angles (illustrated in gray dashed lines). This also confirms that the estimation uncertainty increases as the wall angle deviates away from $\alpha = \pi/2$, because the signal magnitude becomes smaller with respect to the sensor noise. From the comparison, we have the same conclusion that this prototype sensory system is able to estimate the wall distance (if the nominal pressure amplitude is provided) and determine the general orientation of the wall (with respect to the relative moving direction in the fluid).

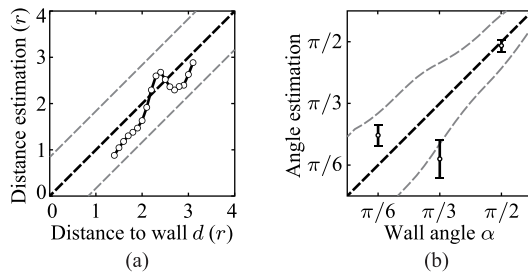


Fig. 19. Comparison between the measurement and the estimation in the experiment test. (a) Estimation of wall distance d . (b) Estimation of wall angle α . The wall distance is provided by the motion capture system and the angle is obtained by design of the setup. The estimation of the wall distance and angle is based on the Fourier analysis of the pressure distribution. The data are obtained from the average of five pairs of tests. The average distance estimation including velocity profile discrepancies generally captures the measurement with a standard deviation of $0.83 r$ (as illustrated by the gray dashed lines). The estimated angle roughly agrees with the actual value, especially considering the modest signal magnitude for the cases with the wall angles $\alpha = \pi/6$ and $\pi/3$. The estimation error has a varying error bound due to the different signal magnitudes with respect to the sensor noise (as illustrated by the gray dashed lines).

V. CONCLUSION

A lateral line inspired pressure sensory system is developed to obtain the pressure distribution and is tested in experiments. The pressure distribution reflects the hydrodynamic information about the surrounding flow. The first order of the distribution, the spatial integration, represents an estimation of hydrodynamic force and moment, which may improve the control performance when provided to an underwater vehicle controller [37]. The higher orders reflect local pressure variations that allow for detection of flow patterns, which in turn leads to detection of obstacles (e.g., a straight wall).

This paper reports on experimental tests on hydrodynamic force estimation and wall detection with the prototype sensory system. By placing differential pressure sensors around the surface of a testing cylinder and obtaining the pressure distribution on the surface, the hydrodynamic force acting on the cylinder is estimated. In the wall detection tests, the cylinder moves toward a flat wall, the existence of the wall, the wall angle with respect to the moving direction, and the wall distance could be inferred by the variations in the pressure distribution. The results from the detection test qualitatively agree with those from the numerical simulation. Undoubtedly, incorporating the sensory system with the autonomous controller on an underwater vehicle could potentially improve the performance of station keeping, docking, and trajectory tracking. The wall detecting capability could be helpful for obstacle avoidance and navigation.

ACKNOWLEDGMENT

The authors would like to thank Dr. M. Krieg, Z. Ren, S. Nason, N. Imponenti, and K. Nelson for their assistance during the experiments, and the anonymous reviewers for their valuable comments and suggestions to improve the quality of this paper.

REFERENCES

- [1] J. H. S. Blaxter, "Structure and development of the lateral line," *Biol. Rev.*, vol. 62, no. 4, pp. 471–514, Nov. 1987.
- [2] H. Bleckmann, "Peripheral and central processing of lateral line information," *J. Comput. Physiol. A, Neuroethol. Sens. Neural Behav. Physiol.*, vol. 194, no. 2, pp. 145–158, Feb. 2008.
- [3] S. Coombs, "Smart skins: Information processing by lateral line flow sensors," *Autonom. Robots*, vol. 11, no. 3, pp. 255–261, Nov. 2001.
- [4] J. C. Montgomery, C. F. Baker, and A. G. Carton, "The lateral line can mediate rheotaxis in fish," *Nature*, vol. 389, pp. 960–963, Oct. 1997.
- [5] T. J. Pitcher, B. L. Partridge, and C. S. Wardle, "A blind fish can school," *Science*, vol. 194, no. 4268, pp. 963–965, Nov. 1976.
- [6] J. C. Montgomery and J. A. Macdonald, "Sensory tuning of lateral line receptors in Antarctic fish to the movements of planktonic prey," *Science*, vol. 235, no. 4785, pp. 195–196, Jan. 1987.
- [7] K. Pohlmann, J. Atema, and T. Breithaupt, "The importance of the lateral line in nocturnal predation of piscivorous catfish," *J. Exp. Biol.*, vol. 207, pp. 2971–2978, Aug. 2004.
- [8] S. Coombs, C. B. Braun, and B. Donovan, "The orienting response of Lake Michigan mottled sculpin is mediated by canal neuromasts," *J. Exp. Biol.*, vol. 204, pp. 337–348, Jan. 2001.
- [9] M. Satou, *et al.*, "Behavioral and electrophysiological evidences that the lateral line is involved in the inter-sexual vibrational communication of the Himé salmon (landlocked red salmon, *Oncorhynchus nerka*)," *J. Comput. Physiol. A, Neuroethol. Sens. Neural Behav. Physiol.*, vol. 174, no. 5, pp. 539–549, May 1994.
- [10] A. B. Kroese, J. M. van der Zalm, and J. van den Bercken, "Frequency response of the lateral-line organ of *Xenopus laevis*," *Pflügers Arch.*, vol. 375, no. 2, pp. 167–175, Jul. 1978.
- [11] A. B. Kroese and N. A. Schellart, "Velocity- and acceleration-sensitive units in the trunk lateral line of the canal," *J. Neurophysiol.*, vol. 68, no. 6, pp. 2212–2221, Dec. 1992.
- [12] M. Krieg, P. Klein, R. Hodgkinson, and K. Mohseni, "A hybrid class underwater vehicle: Bioinspired propulsion, embedded system, and acoustic communication and localization system," *Mar. Technol. Soc. J.*, vol. 45, no. 4, pp. 153–164, Jul. 2011.
- [13] K. Mohseni, "Zero-mass pulsatile jets for unmanned underwater vehicle maneuvering," presented at *3rd AIAA Unmanned Unlimited Technol. Conf., Workshop Exhib.*, Chicago, IL, USA, Sep. 2004.
- [14] K. Mohseni, "Pulsatile vortex generators for low-speed maneuvering of small underwater vehicles," *Ocean. Eng.*, vol. 33, no. 16, pp. 2209–2223, Nov. 2006.
- [15] T. M. Thomas, M. Krieg, and K. Mohseni, "Thrust characterization for bio-inspired pulsatile vortex ring thrusters with variable exit nozzle diameter," presented at *ASME Int. Mech. Eng. Congr. Expo.*, Buena Vista, FL, USA, Nov. 2009.
- [16] M. Krieg and K. Mohseni, "Thrust characterization of pulsatile vortex ring generators for locomotion of underwater robots," *IEEE J. Ocean. Eng.*, vol. 33, no. 2, pp. 123–132, Apr. 2008.
- [17] M. Krieg and K. Mohseni, "Dynamic modeling and control of biologically inspired vortex ring thrusters for underwater robot locomotion," *IEEE Trans. Robot.*, vol. 26, no. 3, pp. 542–554, Jun. 2010.
- [18] Z. Fan, *et al.*, "Design and fabrication of artificial lateral line flow sensors," *J. Micromech. Microeng.*, vol. 12, no. 5, pp. 655–661, Jun. 2002.
- [19] Y. Yang, *et al.*, "Distant touch hydrodynamic imaging with an artificial lateral line," *Proc. Nat. Acad. Sci. USA*, vol. 103, no. 50, 2006, pp. 18 891–18 895.
- [20] A. Dagamseh, R. Wiegerink, T. Lammerink, and G. Krijnen, "Imaging dipole flow sources using an artificial lateral-line system made of biomimetic hair flow sensors," *J. Roy. Soc. Interface*, vol. 10, no. 83, 2013.
- [21] A. Klein and H. Bleckmann, "Determination of object position, vortex shedding frequency and flow velocity using artificial lateral line canals," *Beilstein J. Nanotechnol.*, vol. 2, pp. 276–283, Jun. 2011.
- [22] A. G. P. Kottapalli, M. Asadnia, J. M. Miao, G. Barbastathis, and M. S. Triantafyllou, "A flexible liquid crystal polymer MEMS pressure sensor array for fish-like underwater sensing," *Smart Mater. Struct.*, vol. 21, no. 11, pp. 1–13, 2012.
- [23] A. G. P. Kottapalli, M. Asadnia, J. Miao, and M. S. Triantafyllou, "Touch at a distance sensing: Lateral-line inspired MEMS flow sensors," *Bioinspir. Biomim.*, vol. 9, no. 4, Nov. 2014.
- [24] L. DeVries, F. D. Lagor, H. Lei, X. Tan, and D. A. Paley, "Distributed flow estimation and closed-loop control of an underwater vehicle with a multi-modal artificial lateral line," *Bioinspir. Biomim.*, vol. 10, no. 2, 2015.

- [25] M. E. McConney, *et al.*, “Biologically inspired design of hydrogel-capped hair sensors for enhanced underwater flow detection,” *Soft Matter*, vol. 5, pp. 292–295, 2008.
- [26] A. G. P. Kottapalli, *et al.*, “A liquid crystal polymer membrane MEMS sensor for flow rate and flow direction sensing applications,” *J. Micromech. Microeng.*, vol. 21, no. 8, pp. 1–11, 2011.
- [27] M. S. Triantafyllou, G. D. Weymouth, and J. Miao, “Biomimetic survival hydrodynamics and flow sensing,” *Ann. Rev. Fluid Mech.*, vol. 48, no. 1, pp. 1–24, 2016.
- [28] V. I. Fernandez, *et al.*, “Lateral-line-inspired sensor arrays for navigation and object identification,” *Mar. Technol. Soc. J.*, vol. 45, no. 4, pp. 130–146, Jul./Aug. 2011.
- [29] R. Venturelli, *et al.*, “Hydrodynamic pressure sensing with an artificial lateral line in steady and unsteady flows,” *Bioinspir. Biomim.*, vol. 7, no. 3, pp. 1–12, Apr. 2012.
- [30] A. Gao and M. S. Triantafyllou, “Bio-inspired pressure sensing for active yaw control of underwater vehicles,” in *Proc. OCEANS Conf.*, Oct. 2012, DOI: 10.1109/OCEANS.2012.6404844.
- [31] T. Salumäe and M. Kruusmaa, “Flow-relative control of an underwater robot,” *Proc. Roy. Soc. A*, vol. 469, no. 2153, pp. 1–19, 2013.
- [32] N. Strokina, J. K. Kämäräinen, J. A. Tuhtan, J. F. Fuentes-Pérez, and M. Kruusmaa, “Joint estimation of bulk flow velocity and angle using a lateral line probe,” *IEEE Trans. Instrum. Meas.*, vol. 65, no. 3, pp. 601–613, 2016.
- [33] L. D. Chambers, *et al.*, “A fish perspective: Detecting flow features while moving using an artificial lateral line in steady and unsteady flow,” *J. Roy. Soc. Interface*, vol. 11, no. 99, pp. 1–13, 2014.
- [34] Z. Ren and K. Mohseni, “A model of the lateral line of fish for vortex sensing,” *Bioinspir. Biomim.*, vol. 7, no. 3, May 2012.
- [35] Z. Ren and K. Mohseni, “Wall detection by lateral line sensory system of fish,” presented at 52nd AIAA Aero. Sci. Meeting, National Harbor, MD, USA, Jan. 2014.
- [36] T. I. Fossen, *Guidance and Control of Ocean Vehicles*, New York, NY, USA: Wiley, 1994, pp. 93–113.
- [37] Y. Xu and K. Mohseni, “Bioinspired hydrodynamic force feedforward for autonomous underwater vehicle control,” *IEEE/ASME Trans. Mechatron.*, pp. 1–11, 2013.
- [38] S. P. Windsor, S. E. Norris, S. M. Cameron, G. D. Mallinson, and J. C. Montgomery, “The flow fields involved in hydrodynamic imaging by blind Mexican cave fish (*Astyanax fasciatus*). Part I: Open water and heading towards a wall,” *J. Exp. Biol.*, vol. 213, no. 22, pp. 3819–3831, 2010.



Yiming Xu received the B.S. degree in automation from Zhejiang University, Hangzhou, China and the M.S. degree in mechanical engineering from the University of Florida, Gainesville, FL, USA, where he is currently working toward the Ph.D. degree.

His current research interests include dynamic modeling, nonlinear control design, and stability analysis of multiagent dynamic systems.



Kamran Mohseni (M’06–SM’12) received the B.S. degree from the University of Science and Technology, Tehran, Iran, the M.S. degree in aeronautics and applied mathematics from the Imperial College of Science, Technology, and Medicine, London, U.K., and the Ph.D. degree in mechanical engineering from the California Institute of Technology (Caltech), Pasadena, CA, USA, in 2000.

He was a Postdoctoral Fellow in Control and Dynamical Systems at Caltech for a year and a half before joining the Department of Aerospace Engineering Sciences at the University of Colorado at Boulder in 2001.

In 2011, he joined the University of Florida, Gainesville, FL, USA, as the W.P. Bushnell Endowed Chair in the Department of Electrical and Computer Engineering and the Department of Mechanical and Aerospace Engineering. He is the Director of the Institute for Networked Autonomous Systems.

Dr. Mohseni is a member of the American Society of Mechanical Engineers, the American Physical Society, and the Society for Industrial and Applied Mathematics. He is also an Associate Fellow of the American Institute of Aeronautics and Astronautics.